Article

# Discrete coordination nanochains based on photoluminescent dyes reveal intrachain exciton migration dynamics

Ryojun Toyoda [1] ✉, Naoya Fukui [2] ✉, Haru Taniguchi[1], Hiroki Uratani [3], Joe Komeda[4], Yuta Chiba[1], Hikaru Takaya[5,6], Hiroshi Nishihara [2] & Ryota Sakamoto [1,7] ✉

Elucidating exciton migration in polymer chains has been one of the major research goals in photophysics for over half a century. While great efforts have been made to understand picosecond phenomena by ultrafast spectroscopy, ambiguous molecular conformations and/or random polymer sequences have hindered the construction of an ideal exciton migration model. Here we present the creation of unique end-capped coordination nanochains and quantitative description of intrachain exciton migration therein. The nanochain features unique molecular architectures in discrete polynuclear complexes, with a linear and rigid structure, the defined number of metal nuclei, and charge neutrality. These features allow well-defined arrangement of emissive dye moieties, making the nanochain a sound platform for studying exciton dynamics. Readily accessible absorption spectroscopy, and photoluminescence lifetime and quantum yield measurements allow the construction of continuous-time Markov chains model, thereby estimating non-trivial exciton migration across the metal center.

Over 50 years, researchers have discovered that the random walk theory[1–4] is applicable to nanoscale photophysical phenomena in polymer chains, estimating their exciton hopping behaviors[5–11]. In most of resent study, ultrafast laser spectroscopy plays a key role in disclosing fast exciton dynamics where the time scale of observable phenomena depends on the performance of lasers and detectors. However, the high conformational freedom of typical polymers has hampered the elucidation of quantitative exciton transfer phenomenon. Meanwhile, Wang et al. utilized a designed skeleton of metal-organic frameworks (MOFs) to study exciton diffusion based on a fluorescence resonance energy transfer (FRET) model[12]. Therein,

donor molecules were incorporated into the MOF framework to study on exciton transfer to acceptor molecules adsorbed in its mesopores, although the arrangement of the acceptor molecules is hard to determine. We have previously developed a random coordination copolymer (**P1**, Fig. 1a) based on bis(dipyrrinato)zinc(II) complexes by employing two different dipyrrin bridging ligands (**BL1** and **BL2** as exciton acceptor and donor, respectively)[13]. As the constituents are analogous to well-known FRET-based BODIPY probes[14–19], the copolymers emit bright photoluminescence (PL). Unlike conventional flexible polymers, this series of coordination wires features a robust skeleton, which was visualized by AFM as straight single strands[13,20,21]. This

[1]Department of Chemistry, Graduate School of Science, Tohoku University, 6-3 Aramaki-Aza-Aoba, Aoba-ku, Sendai 980-8578, Japan. [2]Research Institute for Science and Technology, Tokyo University of Science, 2641 Yamazaki, Noda, Chiba 278-8510, Japan. [3]Department of Molecular Engineering, Graduate School of Engineering, Kyoto University, Kyoto 615-8510, Japan. [4]Institute of Nanotechnology (INT), Karlsruhe Institute of Technology (KIT), Hermann-von-Helmholtz-Platz 1, 76344 Eggenstein-Leopoldshafen, Germany. [5]Department of Life & Health Science, Faculty of Life & Environmental Sciences, Teikyo University of Science, Adachi-ku, Tokyo 120-0045, Japan. [6]Institute for Molecular Science, National Institute of Natural Science, Nishigo-Naka, Myodaiji, Okazaki 444-8585, Japan. [7]Division for the Establishment of Frontier Sciences of Organization for Advanced Studies at Tohoku University, 2-1-1 Katahira, Aoba-ku, Sendai 980-8577, Japan. ✉e-mail: ryojun.toyoda.a8@tohoku.ac.jp; n-fukui@rs.tus.ac.jp; ryota.sakamoto.e3@tohoku.ac.jp
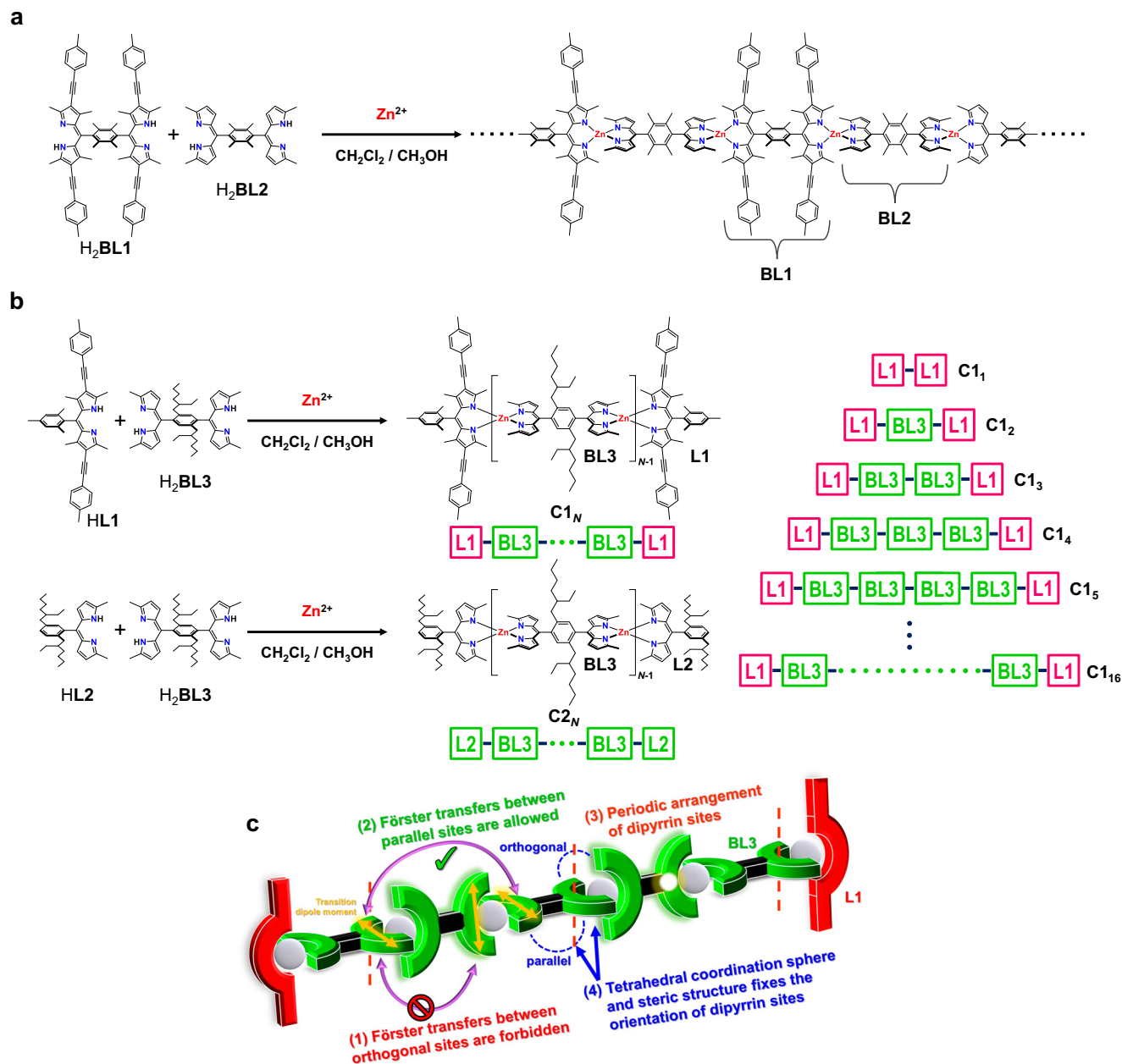
Fig. 1 | Coordination nanochains of this work. a Synthetic scheme of coordination random copolymer **P1**[13]. **b** Synthetic scheme of end-capped coordination nanochains **C1**$_N$ and **C2**$_N$. **c** Molecular design concept of **C1**$_N$ for the purpose of the present work.

feature is beneficial in the study of exciton migration, as structural fluctuation upon bending and folding, which affects the phenomenon largely, is circumvented. Also, the fixed distance and orientation between the dipyrrin moieties and localization of a photogenerated exciton on a dipyrrin in a chain allow for the calculation of Förster-type intramolecular energy transfer rates. With these structural advantages in hand, we performed, to **P1**, a combination of steady-state measurements of photophysical properties and a numerical simulation on photoluminescence (PL) efficiencies with a random walk model, revealing intrachain exciton transfer with an estimated hopping rate of 24–43 ns^{-1} (23–41 ps as a time constant). It is remarkable that contrary to the previous studies with transient spectroscopies, our strategy can understand picosecond phenomena with a combination of steady-state techniques and an easy-to-access nanosecond spectrometer used for PL lifetime measurement. However, the out-of-control coordination reaction in **P1** would generate intrinsically random donor and acceptor arrangements in the copolymer chain, as is similar to other

copolymer systems[13,22–30]. In our previous study, such indefinite arrangements actually compelled us to adopt not only mathematical but also statistical procedures and to neglect several hopping paths. In order to build a more realistic and sophisticated random walk model, precise control of polymer sequences is requested.

In this work, end-capped multinuclear complexes (hereafter called nanochains) **C1**$_N$ (Fig. 1b; N is the number of metal centers, $N = 1$ – 16) are synthesized and isolated in every N. Instead of two bridging ligands **BL1** and **BL2** used in the random copolymer (Fig. 1a), end-capping ligand **L1** and bridging ligand **BL3** are used for the construction of **C1**$_N$ (Fig. 1b). **L1** corresponds to the half structure of **BL1**, thereby behaving as an exciton acceptor. **BL3** is an analog of **BL2** with branched alkyl chain groups introduced at the phenylene linker for the improved solubility of the resulting nanochains, serving as an exciton donor. The complexation of these ligands to zinc(II) ions formed a mixture of end-capped multinuclear complexes, and each discrete coordination nanochain was separated by size-exclusion

chromatography (SEC). Additionally, nanochains $C2_N$ (Fig. 1b; $N=1-10$) were prepared in a similar manner by substituting **L1** with **L2**. $C2_N$ lacks the acceptor dipyrrin unit at the terminus, such that it serves as a reference for $C1_N$ in the exciton migration study. From the viewpoint of coordination chemistry, these nanochains are also characterized as an unparalleled molecular architecture in the category of linear multinuclear complexes. Peng[31,32], Shionoya[33] and Murahashi[34] reported metal-cluster-type complexes where coordination bonds are used for assembling metal ions and do not influence their chain elongation processes. In contrast, discrete coordination chains have been poorly developed. Their main chains are constructed based on coordination bonds, and the molecular strands have defined lengths depending on the number of metal atoms. To the best of our knowledge, $C1_{16}$ is the second largest linear multinuclear complex after Re(I) oligomers bearing 20 complex units reported by Ishitani and coworkers in 2008[35]. However, the one-dimensional structures are intrinsically different with each other: The Re(I) oligomer has winding and deformable structures due to the flexibility of phosphine bridging ligands, while our nanochain has a straight and solid structure thanks to the rigidity of the bidentate dipyrrin bridging ligand (evidenced later). Besides, charge neutrality is another advantage in the nanochain to circumvent electronic perturbation by counterions, while the Re(I) oligomer is cationic. The critical advantage of the nanochain over random copolymer **P1** (Fig. 1a) is that the former has a defined sequence (Fig. 1b). Together with the rigid architecture mentioned above, the structural feature of $C1_N$ allows it to serve as an ideal platform for exciton migration study (Fig. 1c; detail discussed in a later section). Here, the movement of an exciton in nanochain $C1_N$ is described with continuous-time Markov chains (CTMC), a generalized random walk. By constructing a CTMC model for the exciton migration, and simulating PL lifetime and quantum yield measurement data thereby, we can estimate non-trivial exciton transfer across the metal center.

Results

Preparation of end-capped coordination nanochains

In order to obtain nanochain $C1_N$, a dichloromethane (DCM) solution of bridging ligand H_2**BL3** and capping ligand H**L1** in a ratio of 5:2 was prepared, and then a methanol solution of zinc acetate was added to the solution and stirred overnight. As chelation reaction between dipyrrins and zinc(II) ions proceeds spontaneously without adding any base, the resulting mixture is supposed to consist of various multinuclear complexes (e.g., mononuclear, dinuclear, trinuclear, etc) with the capping ligands at both ends of a linear chain (Fig. 1b,c). Without the capping ligand, a powder of the homopolymer (**P2**, Supplementary Fig. 7) is obtained from the reaction mixture as reported in our previous studies[13,20,21]. Therefore, the capping ligand plays an important role in producing discrete complexes as it stops the chain elongation. The reaction mixture was evaporated under vacuum, and the resulting product was dissolved again in chloroform. This solution was then subjected to SEC to separate and purify each product (Supplementary Figs. 9–11). Figure 2a represents the second cycle of SEC, clearly showing the product contains more than ten compounds. Note that the peaks are located regularly, so the mass differences between two adjacent peaks seem constant. This indicates that both ends of the complexes are capped with dipyrrinato capping ligand, **L1**, and the number of bridging ligands is the difference between the complexes. Once after the removal of acetic acid, the complexes are quite stable and ligand dissociation or exchange does not happen as demonstrated in previous studies[13,22–25]. This feature allowed us to isolate the multinuclear complexes and investigate the properties of the individual products. They are thermodynamically produced considering the yield of each nanochain (Supplementary Fig. 12). Similarly, another set of nanochain $C2_N$ was prepared using the capping ligand H**L2** whose dipyrrin structure is the same as those of the bridging ligand. Here all the

complex units become homoleptic which is reminiscent of homopolymer **P2** (Supplementary Fig. 7).

Characterization of coordination nanochains

All the obtained fractions after SEC separation were characterized by ^{1}H NMR spectroscopy. Figure 2b depicts the ^{1}H NMR spectrum for $C1_{10}$ focusing on the aromatic region. In the aromatic region (7.15 – 6.15 ppm), there are peaks derived from the proton of the mesityl group of **L1** (H_a, 6.98 ppm), the phenyl proton of **L1** (H_b, 7.11 – 7.09 ppm), and two kinds of protons at γ and β positions of the **BL3** dipyrrins, H_c (around 6.60 ppm) and H_d (around 6.23 ppm), respectively. Integration of these peaks revealed the ratio of **L1** to **BL3** is 2 to 9, which is consistent with the ideal ratio for decanuclear complex $C1_{10}$. Similarly, the Nth fraction ($N=1-16$) was identified as end-capped dipyrrin-zinc complex $C1_N$ with ($N-1$) bridging ligands (Supplementary Fig. 14). Also, electrospray ionization mass spectrometry (ESI-MS) was used for further characterization of the complexes (Fig. 2c). All the fractions were investigated, and mononuclear to decanuclear complexes ($C1_1 - C1_{10}$) were detected from the corresponding fractions (Supplementary Fig. 15). As the molecular chain becomes longer, it was detected with an increased number of charges. $C1_{10}$ was detected as a 5+ charged ion. Ionization of larger complexes ($C1_{11}$ to $C1_{16}$) was not successful, only detecting their decomposed fragments, probably due to their highly anisotropic structures. However, in addition to the ^{1}H NMR investigation, the regulated location of the SEC peaks and mass detection of up to decanuclear complexes supported the formation of the end-capped 11- to 16-nuclear complexes. These coordination nanochains are unique among discrete metal complexes in that they have robust and straight chain structures, charge neutrality, and monodispersity. In addition, mononuclear to decanuclear complexes were separated in the case of $C2_N$. In order to confirm the orthogonal and linear structure of the coordination nanochain, reference nanochain $C3_N$ ($N=1-4$) was prepared from H**L1** and H_2**BL4** lacking the long and branched alkyl chain (Supplementary Figs. 16,17). The stability of the coordination nanochains in solution and more rigid structure of the bridging ligand **BL4** afforded a single crystal of $C3_2$ suitable for X-ray diffraction analysis. We note the single crystal of $C1_N$ was not obtained due to the existence of the long alkyl chain. The single crystal structure of $C3_2$ disclosed the linearity of the nanochain as designed (Supplementary Fig. 18 and Supplementary Table 1).

Coordination nanochain design

A distinctive structural feature of nanochain $C1_N$ is that the relative conformations of all dipyrrin moieties are orthogonal or parallel. To demonstrate this, we conducted DFT optimization for mononuclear model complex **MC-1** (Fig. 3a,b, Supplementary Table 2) and dinuclear one $C3_2$ (Supplementary Fig. 19 and Supplementary Table 3). **MC-1** is an asymmetric complex constructed from end-capping ligand **L1** and ligand **BL3'**: The latter corresponds to half of bridging ligand **BL3**. The dihedral angle of **MC-1** exhibited the orthogonality at the zinc center, with a dihedral angle of 89.99°. Meanwhile, in $C3_2$, the two dipyrrin ligands belonging to the same bridging ligand feature a parallel conformation to each other (average dihedral angle: 0.00°). The orthogonal and parallel conformation was supported further by the single crystal X-ray structure of $C3_2$, with dihedral angles of 89.42° and 0.00°, although the dipyrrin moiety was perturbed by the crystal packing (Supplementary Fig. 18). Rigidity is another structural feature of $C1_N$. The bidentate coordination of the dipyrrin moiety to the Zn center prevents free rotation at the Zn-N bond. The introduction of methyl groups at the α-position of all dipyrrin moieties prevents structural changes relating to the Zn coordination sphere. The rigidity of the nanochain is ensured by the fact that the linear structure of a single strand of a coordination polymer that contains the nanochain as a substructure was visualized by AFM[20]. Furthermore, the charge neutrality of the bis(dipyrrinato)zinc complex motif is also advantageous,
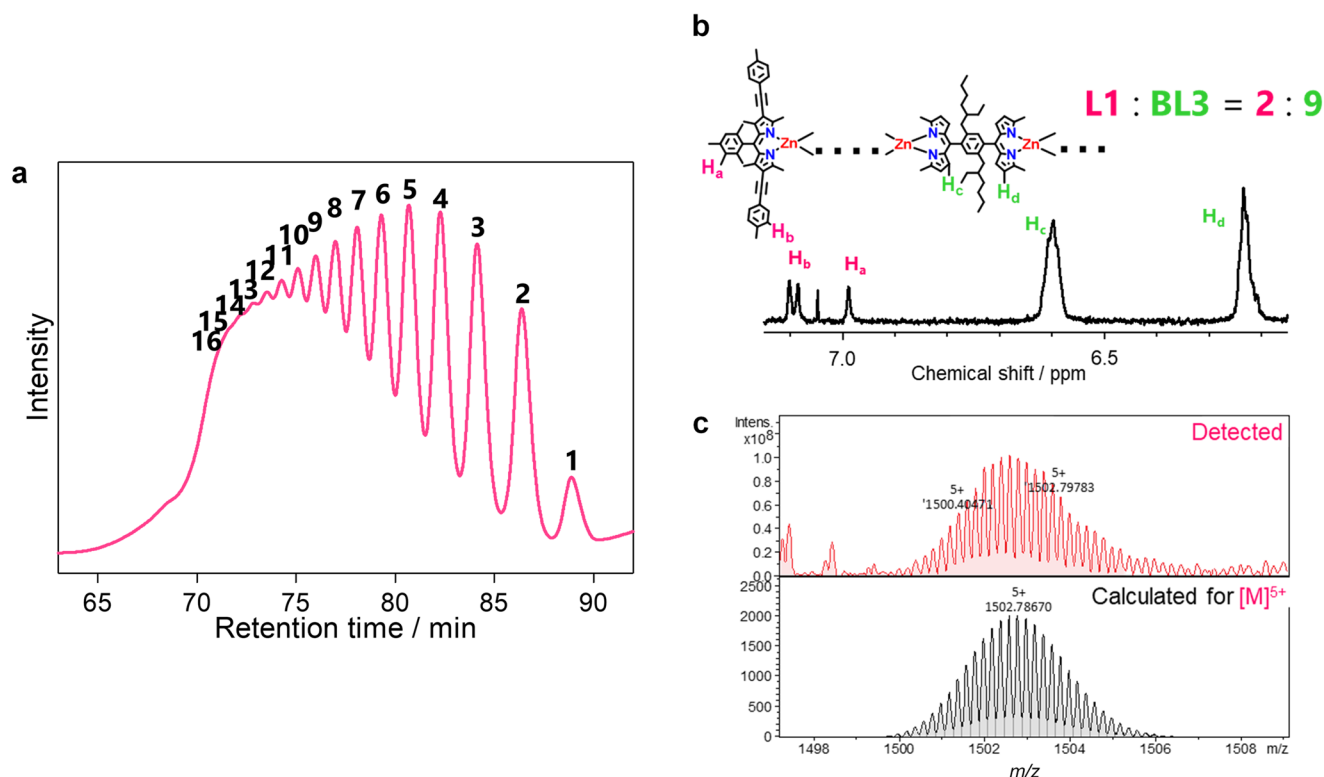
Fig. 2 | Characterization of nanochain C1$_N$. **a** SEC chromatogram of the second cycle of **C1$_N$** separation. **b** Aromatic region of ^{1}H NMR spectrum of **C1$_{10}$** measured in chloroform-*d*. **c** ESI-MS spectrum of **C1$_{10}$** (upper panel) with a calculated spectrum for [M]$^{5+}$ (lower panel).

as it prevents structural perturbation by the counter ions. The orientation of the transition dipole moment of each dipyrrin site is also critical. The lowest transition in a dipyrrin ligand is a π-π* transition, which is reported to be oriented in the long-axis direction (vide infra)[36]. Exciton transfer in the nanochain is in principle based on continuous Förster exciton migration processes. In this scheme, the orientation between the transition dipole moments of two dye moieties, is a critical factor. The structural features of **C1$_N$** and the directionality of the transition dipole moment of the dipyrrin moiety can greatly simplify the exciton hopping model as follows (Fig. 1c). (1) Förster energy transfer between orthogonal dipyrrin sites is neglected with one exception, while that between parallel dipyrrin sites is taken into account. (2) The rigid structure of **C1$_N$** may significantly reduce the number of Förster energy transfer processes to be considered. If molecular chains are flexible, as in common polymers or multinuclear complexes, a huge number of Förster energy transfer processes must be considered depending on possible conformations. (3) The presence of capping ligand **L1** in nanochain **C1$_N$** is also important: PL from **L1** allows us to spectroscopically demonstrate that the exciton reaches the end of the nanochain, which is not possible in the case of nanochain **C2$_N$** lacking **L1**. For these reasons, nanochain **C1$_N$** is a suitable molecular platform for elucidating exciton transfer processes based on the CTMC model; such molecular systems are rarely realized.

UV/vis absorption spectra

Isolated nanochain series **C1$_N$** ($N = 2$–16) were dissolved in toluene, and their UV/vis absorption spectra were measured. The normalized spectra are shown in Fig. 3c. **C1$_N$** has two absorption bands in the visible region, with peak tops at around 490 nm and 554 nm, respectively. As N increases, the relative intensity of the absorption at 554 nm decreases. In addition, the intensity of the absorption peak at 490 nm relative to that at 554 nm increases linearly with $N-1$, the number of bridging ligand **BL3** (Fig. 3d). In contrast, the absorption peak at 554 nm is not observed in the **C2$_N$** series, which does not have **L1**

(Supplementary Fig. 20). Therefore, the absorption bands at 490 nm and 554 nm originate from bridging ligand **BL3** and capping ligand **L1**, respectively. In addition, when compared with the spectra of free-base dipyrrin proligands H$_2$**BL3** (439 nm) and H**L1** (508 nm), which are the starting materials of **C1$_N$**, we notice that both of the two absorption bands of **C1$_2$** undergo redshifts (Supplementary Fig. 21). Such redshifts are characteristic of the formation of a bis(dipyrrinato)zinc complex motif[20]. This series of absorption spectral results also ensures nanochain **C1$_N$** based on coordination bonding is formed and exist stably. Furthermore, the absorption peaks at around 490 nm derived from the bridging ligands are almost identical in **C2$_2$** and **C3$_2$** (Supplementary Fig. 22). The bridging ligand of **C3$_2$** (**BL4**; Supplementary Fig. 16) has a durene linker, the four methyl groups of which provide orthogonality with the dipyrrin moiety[20]. From the spectral comparison and previous finding, we may conclude that the two branched alkyl groups at the 2- and 5-positions of the arene linker of **BL3** are sufficient to maintain the rigidity of the dipyrrin ligand and the orthogonality with the dipyrrin unit[37–40].

Next, we investigated the electronic transitions of nanochain **C1$_N$**. Here we employed model mononuclear complex **MC-1** (Fig. 3a). **MC-1** corresponds to the terminal part of nanochain **C1$_N$**, thereby being a suitable model for the investigation of interest. **MC-1** was synthesized in practice, measuring and comparing its normalized absorption spectrum with that of nanochain **C1$_2$**: It is notable that they are almost identical (Supplementary Fig. 23), indicating the validity of **MC-1** as a model. Electronic transitions corresponding to the photoabsorption of **MC-1** were characterized using time-dependent density-functional theory (TD-DFT) calculations with the level of B3LYP/6-31 G + (d) at the molecular geometry optimized at the ground state with the same level of theory. Figure 3e shows the main molecular orbitals of **MC-1** contributing to the S$_0$-S$_2$ and S$_0$-S$_6$ transitions with large oscillator strengths. The S$_0$-S$_2$ transition is a ^{1}π-π* transition localized in **L1**, and the S$_0$-S$_6$ transition is that localized in **BL3'**, which corresponds to half of bridging ligand **BL3** (Fig. 3a). The contribution of the zinc center to
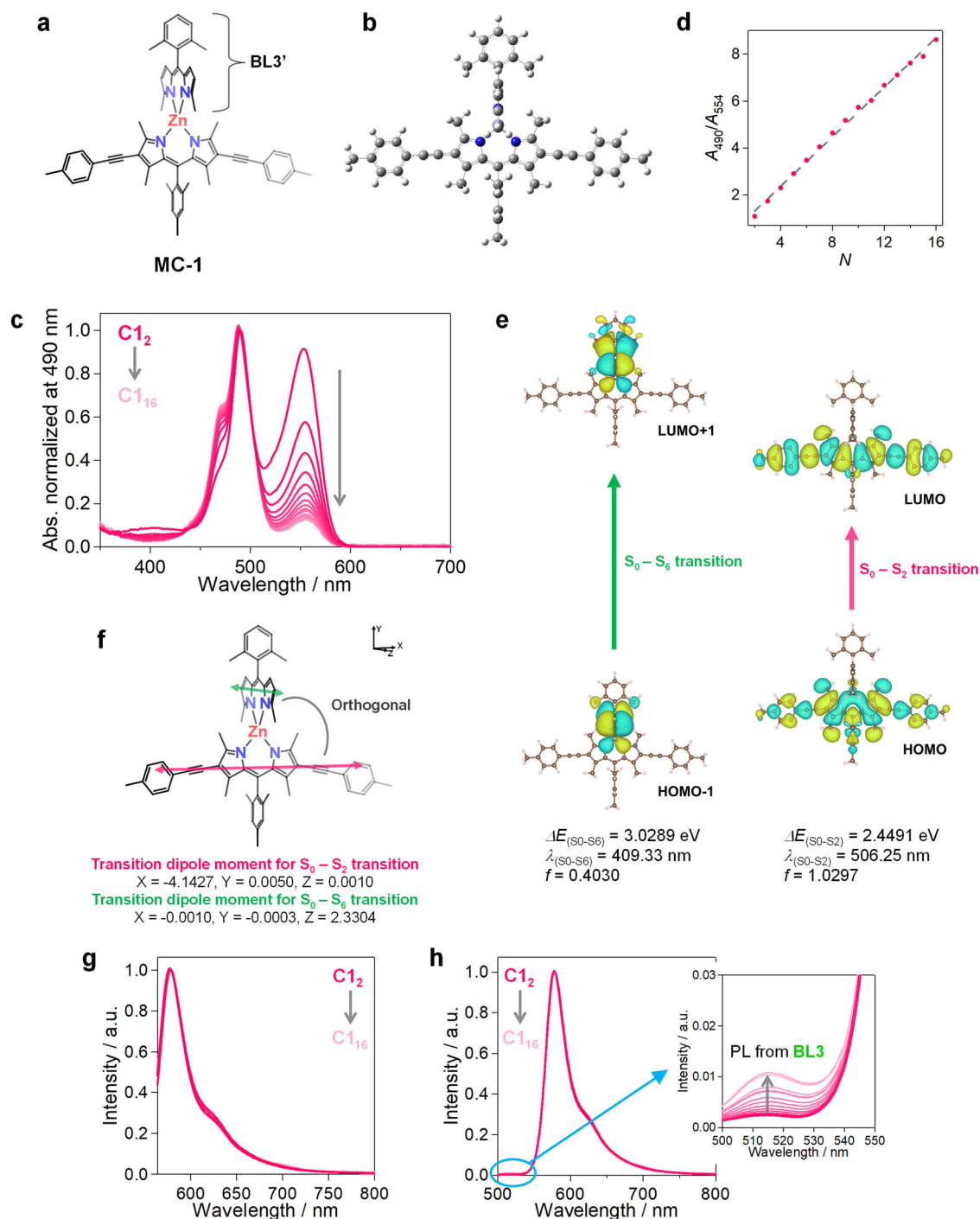
Fig. 3 | Photophysical properties. a Molecular structure of model mononuclear complex **MC-1**. The dipyrrin ligand labeled as **BL3'** is regarded as the half of bridging ligand **BL3**. **b** Optimized structure of **MC-1** by DFT calculation (B3LYP/6-31 g + (d)). **c** Normalized UV/vis absorption spectra of coordination nanochains **C1**$_N$ ($N = 2 - 16$) in toluene. **d** Relationship between the peak ratio of the absorption bands at around 490 nm and 554 nm, and N in **C1**$_N$ ($N = 2 - 16$) in toluene.
e Kohn–Sham occupied and unoccupied orbitals of **MC-1** that chiefly contribute to the $S_0 \rightarrow S_2$ and $S_0 \rightarrow S_6$ transitions calculated at the level of B3LYP/6-31 g + (d).
f Transition dipole moments of **MC-1** for the $S_0 \rightarrow S_2$ and $S_0 \rightarrow S_6$ transitions. **g, h** PL spectra of **C1**$_N$ ($N = 2 - 16$) excited at (**g**) 554 nm and (**h**) 490 nm in toluene.

both transitions is negligible. Supplementary Fig. 24 shows the oscillator strengths and transition energies of the S_0-S_2 and S_0-S_6 absorptions estimated by TD-DFT calculations. S_0-S_2 corresponds to the absorption band at 554 nm, and S_0-S_6 corresponds to that at 490 nm. Note that $S_0 \rightarrow S_1$, $S_0 \rightarrow S_3$, $S_0 \rightarrow S_4$, $S_0 \rightarrow S_5$ possess negligible oscillator strengths (Supplementary Fig. 25). The calculated excitation energies are overestimated compared to the experimental values. We note such overestimation has been frequently reported for dipyrrin-BF$_2$

complexes (BODIPYs), the main transition of which is the $^1\pi$-π^* transition localized at the dipyrrin ligand, similar to dipyrrin-zinc complexes[41]. This series of results indicates the dipyrrin site of **BL3** in **C1**$_N$ can be selectively excited with 490 nm light, whereas that of **L1** can be done with 554 nm light. Figure 3f shows the transition dipole moments of the S_0-S_2 and S_0-S_6 transitions in **MC-1**. Both moments are nearly aligned with the long axis of the dipyrrin ligand. In addition to the orthogonality of the two dipyrrin ligands coordinated to the same

zinc center (Fig. 3b), the two dipole moments were also shown to be orthogonal to each other. Therefore, the design concept for the orientation of the transition dipole moments of $C1_N$ (Fig. 1c) is also verified. The absorption spectra of $C1_N$ and $C2_N$ were comprehensively recorded in toluene, a mixture of toluene and DCM (1:1 v/v), and DCM (Fig. 3c; Supplementary Figs. 26–30).

Steady-state PL

Supplementary Fig. 31 shows the PL spectrum of homopolymer **P2** dispersed in toluene. Therein, **P2** was excited at 490 nm, which is the absorption maximum of constituting bridging ligand **BL3**, to find PL at 512 nm. This PL is derived from either dipyrrin site of **BL3**[20]. Similar PL behavior was found in nanochain $C2_N$ ($N = 2$–10) in toluene (Supplementary Fig. 32), reflecting the structural similarity to **P2**. We also measured the PL spectra of $C2_N$ in a mixture of toluene and DCM (1:1 v/v), and DCM (Supplementary Figs. 33,34), which again detected PL from **BL3**. In contrast, nanochain $C1_N$ exhibited more complex PL behavior. When $C1_N$ ($N = 2$–16) was illuminated with 554 nm light, **L1** got photoexcited directly, and PL from **L1** was observed at 579 nm (Fig. 3g). On the other hand, when $C1_N$ was irradiated with a 490 nm light source, the excitation light is dominantly absorbed by the dipyrrin moieties of **BL3**. Nonetheless, as shown in Fig. 3h, the PL spectra of $C1_N$ upon excitation at 490 nm featured a dominant peak at 579 nm, similar to the case of 554 nm excitation. This indicates most portion of excitons generated at **BL3** transmitted to **L1** located at the terminus of the nanochain before being deactivated at **BL3**. The efficient exciton transfer from **BL3** to **L1** was also supported by the excitation spectra of $C1_N$ monitored at 579 nm (Supplementary Fig. 35). Therein, both the 490 and 554 nm bands contribute to the PL, with a spectral shape and N-dependence similar to the absorption spectra of $C1_N$. When the PL spectra of $C1_N$ upon excitation at 490 nm are enlarged in the range of 500 – 550 nm, we can faintly find PL at 512 nm, the intensity of which slightly grows with N increases (Fig. 3h). This implies the efficient exciton migration from **BL3** to **L1** is slightly deteriorated as the chain length of $C1_N$ increases. Here, interchain exciton migration needs not considering because an exciton in a nanochain decays before another nanochain comes close (SI Section 4.3). Similar PL spectra were obtained for $C1_N$ in other solvents, DCM and a 1:1 mixture of toluene and DCM, showing the absence of significant solvatochromism (Supplementary Figs. 36–38).

PL quantum yield and lifetime

Steady-state PL spectroscopy revealed a qualitative exciton transfer from bridging ligand **BL3** to end-cap ligand **L1** in nanochain $C1_N$. The absolute PL quantum yield (PLQY) and lifetime (τ_{PL}) measurements were then performed to obtain information for the quantitative analysis of the exciton transfer (Fig. 4a-c, Supplementary Tables 4-6) in nanochain $C1_N$ (model is shown in Fig. 4d). Before moving on to nanochain $C1_N$, we first focus on nanochain $C2_N$ that lacks **L1**. Supplementary Figs. 39–41 and Supplementary Tables 7–10 summarize the ϕ_{PL_490} (PLQY upon excitation with 490 nm light) and τ_{PL} values of $C2_N$ ($N = 1$-10). As the polarity of the solvent increases, the ϕ_{PL} value of $C2_N$ decreases. This is because $C2_N$ is composed of homoleptic bis(dipyrrinato)zinc complex units, which were reported to exhibit PL quenching in polar solvents[22,23,25]. ϕ_{PL_490} did not show significant N dependence, except for $C2_1$, which does not have bridging ligand **BL3**. Neither solvent nor N value dependence was observed for τ_{PL} (Supplementary Table 10). These results indicate that the oligomerization of bis(dipyrrinato)zinc complex to form the nanochain does not significantly change the luminescence property. However, $C2_N$ does not provide any evidence for the intrachain exciton hopping. Figure 4a summarizes the ϕ_{PL_490} and ϕ_{PL_554} (PLQY upon excitation with 554 nm light) values of $C1_N$ ($N = 1$-16) measured in toluene. With incident light at 554 nm, π-extended ligand **L1** at the end of the nanochain is selectively excited. **L1** has a lower enough excitation energy than the

dipyrrin site of **BL3** (Fig. 3c, e), and as a result, the exciton stays and decays at **L1**, resulting in ϕ_{PL_554} with a small N dependence (Fig. 4a, orange plots). With 490 nm excitation, an exciton is generated at one of the dipyrrin moieties of **BL3**. This exciton can transfer to another dipyrrin site of **BL3**, and by repetitive exciton transfer, a part of the exciton reaches terminal **L1**, which is detected as PL from **L1**. We show that in toluene, the ϕ_{PL_490} values are almost the same as ϕ_{PL_554} (Fig. 4a, blue plots). This means that in toluene, the exciton transfer from **BL3** to **L1** is almost quantitative. In contrast, in the toluene/DCM mixed solvent, the ϕ_{PL_490} value becomes smaller than ϕ_{PL_554} as N increases (Fig. 4b). The N dependence in ϕ_{PL_490} is more pronounced in DCM (Fig. 4c). This series of results implies that in polar solvents, a part of excitons is deactivated on **BL3** before reaching the **L1** terminus. No significant solvent or N value dependence was observed for τ_{PL} of $C1_N$ (Supplementary Table 6), but there appeared an important difference in the PL decay curves used to calculate τ_{PL}. Figure 4e–g show those of $C1_N$ upon **BL3** excitation at 470 nm in the three solvents (toluene, toluene/DCM (1:1 v/v), and DCM) for $N = 2$, 9, and 13. The comprehensive data for all N are assembled in Supplementary Fig. 42. As N increases, the rise and decay of the PL is delayed, which is the most prominent in DCM, and then a mixture of toluene and DCM. Such a delay was not at all observed for $C2_N$ (Supplementary Fig. 43). The delay in the PL decay curve for $C1_N$ is explained qualitatively as follows. When a typical fluorescent molecule is excited with a pulsed light source, PL is observed immediately after excitation. In sharp contrast, when $C1_N$ is excited at 470 nm, an exciton is generated at one of the dipyrrin sites in bridging ligand **BL3**. It takes more or less time for the exciton to reach end-cap ligand **L1**. In this case, a delay is observed in the PL decay curve according to the rate of exciton transfer from **BL3** to **L1**. The fact that the delay becomes more pronounced as N increases supports the above explanation. In addition, the delay with increasing N is toluene < toluene/DCM mixed solvent < DCM, suggesting that exciton transfer is slower in polar solvents. We then expect the delay should contain quantitative information of the exciton hopping kinetics in nanochain $C1_N$ (vide infra).

Quantification of exciton hopping

In the previous two sections, steady-state PL, PL quantum yield, and fluorescence lifetime measurements were performed on nanochains $C1_N$ and $C2_N$, and qualitatively demonstrated the existence of exciton transfer from bridging ligand **BL3** to end-capping ligand **L1**. In this section, we attempt to quantitatively and mathematically analyze the exciton hopping behavior in $C1_N$ exploiting the experimental data. The outline of the model adopted here is shown in Fig. 4d. $C1_N$ has $2N$ dipyrrin sites arranged in one-dimension, with the two terminal ones belonging to **L1** (Sites 1 and $2N$; red part in Fig. 4d) and the remaining $2(N$-1) ones belonging to **BL3** (Sites 2, 3…$2N$-1; green parts in Fig. 4d). Upon excitation at 490 nm, the exciton occupies one of the dipyrrin sites derived from **BL3**. As time elapses, the exciton undergoes transfer or deactivation following four processes: (1) radiative deactivation ($k_{r\text{-}L1}$ and $k_{r\text{-}BL3}$), (2) non-radiative deactivation ($k_{nr\text{-}L1}$ and $k_{nr\text{-}BL3}$), (3) distant migration by Förster energy transfer ($k_{F[i,j]}$: rate constant for exciton migration from site i to site j; chief ones are illustrated in Fig. 4d; a more detailed description is given in Supplementary Fig. 44), and (4) nearest-neighbor hopping between the dipyrrin sites coordinating to the same zinc ion ($k_{h\text{-}in}$: between dipyrrin sites both belonging to **BL3**, $k_{h\text{-}end}$: from **BL3** to **L1**). Here, k_m is the first-order rate constant for process m. The probability that the exciton moves to another dipyrrin site or disappears by process m during an infinitesimal time Δt is $k_m \Delta t$. Two constraints are imposed to the exciton transfer based on experimental and theoretical facts. First, because the difference in excitation energy is sufficiently larger than the room temperature energy (Fig. 3c,e), exciton transfer from **L1** to **BL3** is prohibited. Second, theoretical requirements dictate that Förster energy transfer between dipyrrin sites with parallel
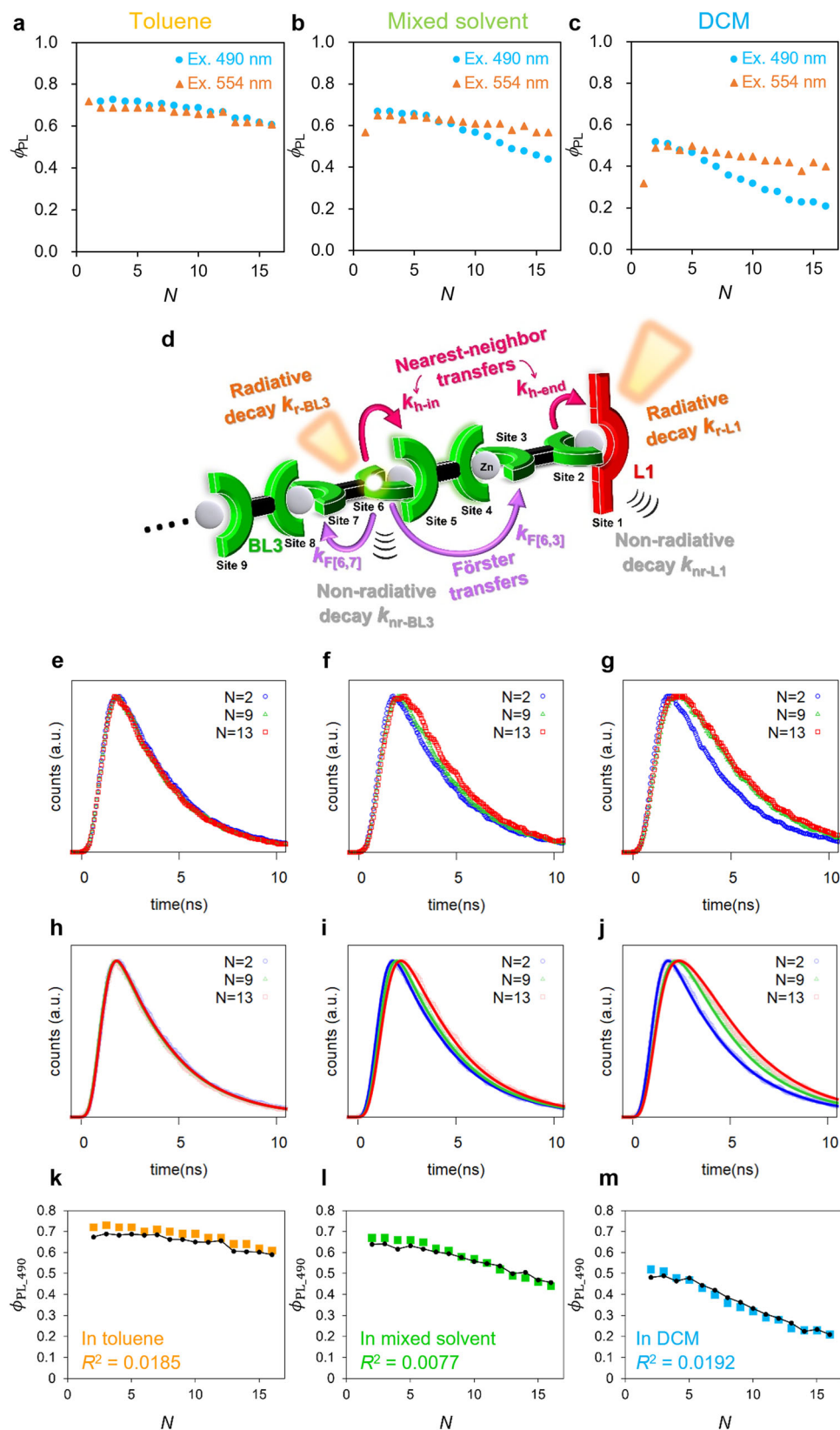
Fig. 4 | PL data and exciton migration dynamics. a–c ϕ_{PL_490} and ϕ_{PL_554} of **C1$_N$** (N = 1–16) in toluene (**a**), toluene/DCM (1:1 v/v) mixed solvent (**b**), and DCM (**c**). **d** Brief illustration of the CTMC model with major exciton decay and transfer processes. Nearest-neighbor exciton migrations over a zinc center $k_{h\text{-in}}$ and $k_{h\text{-end}}$, Förster-type exciton transfers ($k_{F[i,j]}$), radiative ($k_{r\text{-L1}}$ and $k_{r\text{-BL3}}$) and non-radiative ($k_{nr\text{-L1}}$ and $k_{nr\text{-BL3}}$) decays. See Supplementary Fig. 44 for more detail. **e–g** PL decay curves of **C1$_N$** (N = 2, 9, 16) in toluene (**e**), mixed solvent (**f**), and DCM (**g**). The samples were excited at 470 nm. The PL decay curve is smoothed for clarity (the raw decay curve is available in Supplementary Figs. 42, 50–52). **h–j** Simulated decay curves by the CTMC model in toluene (**h**), mixed solvent (**i**), and DCM (**j**). The experimental data are overlaid as open shapes with faint colors. **k–m** Experimental (color squares) and simulated (black dots) ϕ_{PL_490}-N plots of **C1$_N$** in toluene (**k**), mixed solvent (**l**), and DCM (**m**). R^2 is the residual sum of squares.

orientation is permitted, while that between dipyrrin sites with perpendicular orientation is forbidden (Fig. 1c and Supplementary Fig. 44). However, exciton hopping is permitted between nearest-neighbor dipyrrin sites coordinating to the same Zn center, even though they are perpendicular to each other. This exception corresponds to Process (4), which is supported by the experimental fact that efficient inter-ligand exciton transfer was observed in asymmetric bis(dipyrrinato)zinc complexes[22,23]. Note that the above model requires that excitons do not exhibit coherence because it ignores quantum-mechanical effects such as the superposition of states. The incoherent nature of excitons in the nanochains treated in this study was discussed in the Supplementary information (SI Section 4.5; Supplementary Figs. 45–49).

Excitons that undergo transfer or deactivation on a one-dimensional chain according to the probability set at each site may be described by CTMC[42]. $2N$-dimensional vector $\boldsymbol{x}(t)$, which describes the exciton existence probability at the i th ($i = 1, 2, ..., 2N$) dipyrrin site at time t, evolves over time according to the following master equation:

$$\frac{d\boldsymbol{x}(t)}{dt} = A\boldsymbol{x}(t) = \left(A^{\text{rad}} + A^{\text{F}} + A^{\text{hop}} \right)\boldsymbol{x}(t) \quad (1)$$

Here, A is a time-independent $2N \times 2N$ square matrix that describes all transfer and deactivation in $\mathbf{C1}_N$ discussed above. A is the sum of three matrices, A^{rad} describing radiative and non-radiative deactivation, A^{F} describing Förster exciton transfer, and A^{hop} describing the nearest-neighbor hopping. The matrix elements of A^{rad}, A^{F}, and A^{hop} contain rate constants k_{m} explained above as (1)-(4) (see Numerical simulation with the CTMC model in Method section for the detail). Among the rate constants, $k_{\text{h-in}}$ and $k_{\text{h-end}}$ are difficult to quantify from the spectroscopic data obtained thus far, thereby being unknown parameters in this study. By solving Eq. 1, $\boldsymbol{x}(t)$ at any time t can be obtained. From $\boldsymbol{x}(t)$, the PL decay curve of $\mathbf{C1}_N$ during the fluorescence lifetime measurement can be simulated (Fig. 4e-g). Since $\boldsymbol{x}(t)$ includes $k_{\text{h-in}}$ and $k_{\text{h-end}}$, they were determined by fitting the fluorescence decay curve. In other words, the determination of

Table 1 | Time constants of C1₉ calculated from the theoretical model

	Toluene	Mixed solvent	DCM
$\tau_{\text{h-end}}$ (ps)	90 ± 40	45 ± 20	40 ± 30
$\tau_{\text{h-in}}$ (ps)	40 ± 20	26 ± 7	>4000
$\tau_{\text{r-}\mathbf{L1}}$ (ns)	4.0 ± 0.4	4.4 ± 0.5	6.6 ± 0.7
$\tau_{\text{nr-}\mathbf{L1}}$ (ns)	8.1 ± 0.9	7.2 ± 0.8	5.4 ± 0.6
$\tau_{\text{r-}\mathbf{BL3}}$ (ns)	21 ± 2	$3.6 \pm 0.4 \times 10^2$	$4.5 \pm 0.5 \times 10^2$
$\tau_{\text{nr-}\mathbf{BL3}}$ (ns)	3.4 ± 0.4	2.7 ± 0.3	2.2 ± 0.2
$\tau_{\text{F}[2,3]}$ (ps)	0.11 ± 0.01	2.4 ± 0.3	4.6 ± 0.5
$\tau_{\text{F}[3,6]}$ (ps)	13 ± 1	$2.8 \pm 0.3 \times 10^2$	$5.3 \pm 0.6 \times 10^2$
$\tau_{\text{F}[2,6]}$ (ps)	$1.2 \pm 0.1 \times 10^2$	$2.6 \pm 0.2 \times 10^3$	$5.0 \pm 0.4 \times 10^3$
$\tau_{\text{F}[2,7]}$ (ps)	$6.1 \pm 0.4 \times 10^2$	$1.3 \pm 0.1 \times 10^4$	$2.5 \pm 0.2 \times 10^4$
$\tau_{\text{F}[3,10]}$ (ps)	$2.8 \pm 0.2 \times 10^3$	$6.1 \pm 0.4 \times 10^4$	$1.2 \pm 0.1 \times 10^5$
$\tau_{\text{F}[2,10]}$ (ps)	$7.7 \pm 0.6 \times 10^3$	$1.7 \pm 0.1 \times 10^5$	$3.2 \pm 0.2 \times 10^5$
$\tau_{\text{F}[4,1]}$ (ps)	1.8 ± 0.1	34 ± 2	62 ± 4
$\tau_{\text{F}[5,1]}$ (ps)	17 ± 1	$3.2 \pm 0.2 \times 10^2$	$5.8 \pm 0.4 \times 10^2$
$\tau_{\text{F}[8,1]}$ (ps)	$3.9 \pm 0.3 \times 10^2$	$7.4 \pm 0.5 \times 10^3$	$1.3 \pm 0.1 \times 10^4$
$\tau_{\text{F}[9,1]}$ (ps)	$1.1 \pm 0.1 \times 10^3$	$2.0 \pm 0.1 \times 10^4$	$3.7 \pm 0.3 \times 10^4$

$\tau_{\text{h-end}}$: time constant of the nearest-neighbor hopping to **L1**, $\tau_{\text{h-in}}$: time constant of nearest-neighbor hopping between **BL3**, $\tau_{\text{r-}\mathbf{L1}}$: radiative decay at **L1**, $\tau_{\text{nr-}\mathbf{L1}}$: nonradiative decay at **L1**, $\tau_{\text{r-}\mathbf{BL3}}$: radiative decay at **BL3**, $\tau_{\text{nr-}\mathbf{BL3}}$: nonradiative decay at **BL3**, $\tau_{\text{F}[i,j]}$: Förster transfer from the i th to the j th dipyrrin sites. $\tau_{\text{F}[i,1]} = \tau_{\text{F}[2N-i+1, 2N]}$ refers to the Förster transfer to **L1**. Otherwise, $\tau_{\text{F}[i,j]} = \tau_{\text{F}[i+2,j+2]} = \tau_{\text{F}[2N-i+1,2N,j+1]}$ refers to that within the **BL3** chain.

$k_{\text{h-in}}$ and $k_{\text{h-end}}$ is the purpose of constructing the exciton model (Fig. 4d) and numerical analysis by CTMC. For the detail of the fitting method, see Numerical simulation with the CTMC model in Method section, and Section 4.6 and Section 5 in Supplementary information. The PL curves in toluene, toluene/DCM mixed solvent, and DCM were well reproduced along with the delay of the rise (Fig. 4h-j; Supplementary Figs. 50–52). Furthermore, with known $k_{\text{h-in}}$ and $k_{\text{h-end}}$, the $\phi_{\text{PL\_490}}$–N plot (Fig. 4a-c) can be also calculated in the scheme of the CTMC model, and was actually well reproduced when we use the same $k_{\text{h-in}}$ and $k_{\text{h-end}}$ as obtained by the PL decay fitting (Fig. 4k-m). The rate constants of the exciton transfer and deactivation processes in $\mathbf{C1}_9$ in the three solvents are summarized in Table 1 in the form of time constant τ_{m} ($=1/k_{\text{m}}$): Comprehensive time constants and Förster radii (used to calculate $k_{\text{F}[i,j]}$, see Numerical simulation with the CTMC model in Method section for detail) for all $\mathbf{C1}_N$ series were assembled in Supplementary Figs. 53–63 and Supplementary Tables 11–19. As mentioned above, the unknown parameters in the CTMC model are $\tau_{\text{h-in}}$ and $\tau_{\text{h-end}}$. Of these, $\tau_{\text{h-end}}$ was shown to be valid by comparing the photophysical parameters of known asymmetric bis(dipyrrinato)zinc complexes (See Supplementary Fig. 64 and Section 5.3 in Supplementary Information). On the other hand, experimental verification of $\tau_{\text{h-in}}$ is tough because the donor and acceptor are the same chromophore therein. Paradoxically, we may argue that the construction of the exciton hopping model and CTMC analysis thereof succeeded in estimating $\tau_{\text{h-in}}$, which is difficult to estimate. In the model of particle hopping between discrete sites with certain probabilities, the diffusion constant is defined as $D = (\Delta d)^2/2\tau$. Δd is the site spacing, which in this study is 12.5 Å, the spacing between two adjacent zinc ions[13,20]. τ is the time constant of the dominating transfer process. In the case of $\mathbf{C1}_N$, $\tau_{\text{F}[3,6]}$ and $\tau_{\text{h-in}}$ are dominant, such that the contributions of both are added together to evaluate $D = \frac{(\Delta d)^2}{2}\left(\frac{1}{\tau_{\text{F}[3,6]}} + \frac{1}{\tau_{\text{h-in}}}\right)$. $D = 7.3\text{-}9.2 \times 10^{-4}$, $3.2\text{-}3.3 \times 10^{-4}$, and $1.5\text{-}1.8 \times 10^{-5}\,\text{cm}^2\text{s}^{-1}$ in toluene, a mixture of toluene/DCM, and DCM, respectively. These are in the range of diffusion constants for excitons in organic molecular systems reported thus far[43]. The diffusion lengths of an exciton in $\mathbf{C1}_N$, $l_{\text{D}} = (D\tau_{\text{PL}})^{1/2}$, were calculated using D and the fluorescence lifetime of **BL3** to be $l_{\text{D}} = 146\text{-}164$, 93-94, and 18-20 Å in toluene, a mixture of toluene/DCM, and DCM, respectively. These values correspond to ~12, 7, and 2 molecules of bridging ligand **BL3**. The exciton may travel approximately the diffusion length until it is deactivated, which is consistent with the N dependence of $\phi_{\text{PL\_490}}$ (Fig. 4a–c). Thus, a non-polar environment is more favorable for the efficient exciton transport in $\mathbf{C1}_N$.

Coordination nanochains and CTMC model for more precise description on exciton migration

In the previous work[13], the degree of polymerization of copolymer **P1** (Fig. 1a), and the arrangement of bridging ligands **BL1** and **BL2** therein, which act as an exciton donor and an acceptor, respectively, were random. Therefore, we prepared 1000 virtual molecular strands with 2000 dipyrrin sites as a model of **P1** with a sufficiently long chain length. Numerical simulation was then applied to each strand, with the number of exciton hopping in the strand as a variable parameter. A critical problem of the previous model is there was no theoretical or mathematical support for the determination of the time constant of exciton transfer between dipyrrin sites coordinating to the same zinc ion (corresponding to $\tau_{\text{h-in}}$ and $\tau_{\text{h-end}}$ in the present study), only to adopt a plausible but arbitrary value. In the present study, instead of the random copolymer, the strategy of synthesizing nanochains $\mathbf{C1}_N$ was adopted. $\mathbf{C1}_N$ was isolated with defined chain lengths ($N = 2$-16), and the number of **BL3** acting as exciton donors may be accurately determined. In addition, end-capping ligand **L1**, which functions as an exciton acceptor, is located only at both ends. It is not realistic to apply the analytical approach based on CTMC employed in the present work

to the previous random copolymer. The computational cost of calculating the inverse matrix of A in Eq. 1 is proportional to the cube of the number of dipyrrin sites[44]. Furthermore, because of the random structure of the copolymer, analytical solutions must be obtained for a huge number of copolymer strands with different arrangements, and their average value should be adopted. In other words, applying the CTMC approach to random copolymers incurs huge computational costs. By using nanochain $C1_N$ with the above structural characteristics, we were able to calculate $\tau_{\text{h-in}}$ and $\tau_{\text{h-end}}$ analytically by the CTMC method. The PL decay curve and $\phi_{\text{PL\_490}}$-N plot are described as functions of $\tau_{\text{h-in}}$ and $\tau_{\text{h-end}}$. By fitting the simulated PL decay curve with the experimental ones with additional verification by the $\phi_{\text{PL\_490}}$-N plot, we may determine $\tau_{\text{h-in}}$ and $\tau_{\text{h-end}}$, which are difficult to calculate from the spectroscopic data, without the use of ultrafast spectroscopy using fs lasers.

Discussion

Discrete multinuclear complexes, or coordination nanochains were prepared by mixing a terminal ligand and a bridging ligand with a zinc ion. Thanks to the stable complex motif of bis(dipyrrinato)zinc(II), each molecular nanochain could be isolated from the reaction mixture by SEC, affording up to a 16-nuclear complex. They are characterized as unique multinuclear complexes due to their discrete straight-chain structures, orthogonal arrangement of the dye planes, and charge neutrality. The defined ligand sequences of the multinuclear nanochains allowed the construction of a realistic theoretical model for mathematical analysis of exciton behaviors. Analytical calculation based on a CTMC model afforded time constants for exciton migrations in the molecular chains including the non-Förster process. Through this work, we made a large leap in our strategy for evaluating photophysical dynamics in molecular nanomaterials. As our approach is not limited by the performance of lasers and detectors for ultrafast spectroscopy, it is expected to be the key to the new era of photochemistry and photophysics.

Methods

Synthesis of coordination nanochains $C1_N$

A 10 mL of methanol solution of zinc(II) acetate (19.78 mg, 107.8 μmol) was added to a DCM solution (30 mL) of bridging ligand H_2BL3 (52.66 mg, 81.9 μmol) and capping ligand $HL1$ (17.41 mg, 31.8 μmol). After stirring the mixture overnight, the solvent was removed in vacuo. The crude material was diluted with chloroform and separated by SEC to give $C1_N$ ($N=1-16$). Each coordination nanochain was subject to the second SEC separation for further purification.

Synthesis of coordination nanochains $C2_N$

A 10 mL of methanol solution of zinc(II) acetate (42.3 mg, 231 μmol) was added to a DCM solution of $HL2$ (52.3 mg, 111 μmol) and H_2BL3 (41.2 mg, 64.1 μmol). After stirring for 48 h, the solvent was removed in vacuo. The crude material was diluted with chloroform and separated by SEC to give $C2_N$ ($N=1-10$). Each coordination nanochain was subject to the second SEC for further purification.

Numerical simulation with the CTMC model

Here we consider exciton migration in nanochain $C1_N$ with $2N$ dipyrrin sites based on the CTMC model. The distribution of the exciton on a single nanochain $\boldsymbol{x}(t)=(x_1(t),\ \ldots,\ x_{2N}(t))$ evolves with time as:

$$\frac{d\boldsymbol{x}(t)}{dt} = A\boldsymbol{x}(t). \tag{2}$$

Exciton transition probability matrix A is expressed as the sum of three matrices, A^{rad}, A^{hop}, and A^{F}.

A^{rad} is a matrix describing the dissipation related to radiation. Its elements are written as:

$$A_{i,j}^{\text{rad}} = -(k_{\text{r},i} + k_{\text{nr},i})\delta_{i,j} \tag{3}$$

where $k_{\text{r},i}$ and $k_{\text{nr},i}$ are the rate constants for radiative and non-radiative relaxation at the i th dipyrrin unit, and $\delta_{i,j}$ is Kronecker delta. $k_{\text{r},i}$ and $k_{\text{nr},i}$ are defined as follows:

$$k_{\text{r},i} = \begin{cases} k_{\text{r-}L1} & (i=1,\ 2N) \\ k_{\text{r-}BL3} & (\text{otherwise}) \end{cases} \tag{4a}$$

$$k_{\text{nr},i} = \begin{cases} k_{\text{nr-}L1} & (i=1,\ 2N) \\ k_{\text{nr-}BL3} & (\text{otherwise}) \end{cases} \tag{4b}$$

where $k_{\text{r-}L1}$ and $k_{\text{nr-}L1}$ were obtained from the PLQY and PL lifetime of $C1_N$, while $k_{\text{r-}BL3}$ and $k_{\text{nr-}BL3}$ from the PLQY and PL lifetime of $C2_N$. Since $C2_N$ could be isolated from $N=1$ to 10, the measurement was not performed for $N=11$ to 16. Therefore, to gain the $k_{\text{r-}BL3}$ and $k_{\text{nr-}BL3}$ values of $N=11$ to 16, the data for $N=2-10$ were extrapolated linearly. Comprehensive rate constants for the radiative and non-radiative relaxation with errors for all $C1_N$ series (as time constants) are assembled in Section 5.4 in Supplementary Information and Supplementary Figs. 53–56, and Supplementary Tables 11–14.

A^{hop} is a matrix describing the exciton hopping between the dipyrrin unit coordinating to the same zinc center. Its off-diagonal elements are written as:

$$A_{i,i+1}^{\text{hop}} = \begin{cases} k_{\text{h-end}} & (i=1) \\ k_{\text{h-in}} & (i=2..2N-2) \\ 0 & (i=2N-1) \end{cases} \tag{5a}$$

$$A_{i+1,i}^{\text{hop}} = \begin{cases} 0 & (i=1) \\ k_{\text{h-in}} & (i=2..2N-2) \\ k_{\text{h-end}} & (i=2N-1) \end{cases} \tag{5b}$$

where $k_{\text{h-end}}$ is the rate constant of the nearest-neighbor exciton hopping from $BL3$ to $L1$, both of which coordinate to the same zinc center, while $k_{\text{h-in}}$ is that between two $BL3$ ligands. $k_{\text{h-end}}$ and $k_{\text{h-in}}$ are unknown parameters that are hardly determined by the experimental photophysical data. The other off-diagonal elements are 0. The diagonal elements of A^{hop} are written as:

$$A_{i,i}^{\text{hop}} = -\sum_{j\neq i} A_{j,i}^{\text{hop}} \tag{6}$$

A^{F} is a matrix describing Förster exciton transfer. Its elements are written as:

$$A_{j,i}^{\text{F}} = k_{\text{F}[i,j]} = \begin{cases} (k_{\text{r},i}+k_{\text{nr},i})\alpha_i\beta_{i,j}\left(\frac{R_{\text{F},j}}{r_{ij}}\right)^6 & (i\neq j) \\ -\sum_{m\neq i} A_{m,i}^{\text{F}} & (i=j), \end{cases} \tag{7}$$

where $k_{\text{F}[i,j\neq i]}$ is the Förster exciton transfer rate constant from i th to j th dipyrrin units, and $R_{\text{F},j}$ is the Förster radius when the j th dipyrrin unit serves as an acceptor. The Förster radius between a donor dipyrrin site and an acceptor one is calculated from the experimental spectroscopic data using the following equation[45];

$$R_{\text{F}} = 0.211\left[\frac{\kappa^2\phi_D J}{n^4}\right]^{\frac{1}{6}} \tag{8}$$

where R_{F} is the Förster radius in Å, κ is the transition dipole orientation factor and set to 2 (parallel) or 0 (perpendicular), ϕ_D is the quantum

yield of the donor, n is the refractive index of the solvent, and J is the spectral overlap integral determined by Eq. 9;

$$J = \int f_D(\lambda)\epsilon_A(\lambda)\lambda^4 d\lambda \tag{9}$$

where $f_D(\lambda)$ is the emission spectra of the donor (*i.e.*, **C2**$_N$ with the corresponding number of nuclei) normalized to an area of 1, and $\epsilon_A(\lambda)$ is the molar extinction coefficient of the acceptor in M^{-1} cm^{-1} (**L1** analog or half of **BL3**), which was extracted from previous reports[20,23]. λ is in nm. The J values for the exciton transfer from the dipyrrin site of **BL3** to that of **L1** ranged 4.27–4.34 × 10^{15}, 3.46–3.56 × 10^{15}, and 2.13–2.20 × 10^{15} M^{-1} cm^{-1} nm^4 in toluene, a mixture of toluene and DCM (1:1 v/v), and, DCM, respectively. The J values for the exciton transfer between the two dipyrrin sites of **BL3** ranged over 5.62–6.30 × 10^{14}, 3.01–4.28 × 10^{14}, and 2.36–2.69 × 10^{14} M^{-1} cm^{-1} nm^4 in toluene, a mixture of toluene and DCM (1:1 v/v), and, DCM, respectively. Comprehensive Förster radii ($R_{F,\textbf{BL3}}$ and $R_{F,\textbf{L1}}$ where the dipyrrin sites of **BL3** and **L1** are the acceptor, respectively) with errors for all **C1**$_N$ series are assembled in Section 5.4 in Supplementary Information and Supplementary Figs. 57, 58, and Supplementary Tables 15, 16. α_j in Eq. 7 is 0 for $j = 1$ or $2N$, and otherwise 1: This condition prohibits an exciton transfer from **L1** to **BL3**. $\beta_{i,j}$ is the orientation factor and equal to 1 or 0 when the i th and j th dipyrrin sites with are parallel or perpendicular, respectively. For instance, the two dipyrrin sites in **BL3** are parallel to each other, while the two dipyrrin sites that coordinate to the same zinc ion are perpendicular (Fig. 1c). r_{ij} denotes the distance between the i th and j th dipyrrin sites. Based on our previous report on bis(dipyrrinato)zinc coordination polymers[13,20], we set the distance between two dipyrrin sites coordinating to the same zinc atom to 4.7 Å, and that between two dipyrrin sites belonging to the same **BL3** to 7.8 Å. These distances were extracted from an optimized nanochain structure from DFT calculation assuming that the center of dipyrrin is located at the midpoint between the two β-carbon atoms. Thanks to the periodic and rigid structure of **C1**$_N$, $k_{F[i,j]}$ may be simplified: For example, $k_{F[2,3]} = k_{F[4,5]} = k_{F[6,7]}$, $k_{F[3,6]} = k_{F[7,10]}$. Chief Förster exciton transfer rate constants $k_{F[i,j]}$ with errors for all **C1**$_N$ series (as time constants) are assembled in Section 5.4 in Supplementary Information and Supplementary Figs. 59–63, and Supplementary Tables 17–19.

For example, in the case of $N = 3$, the full expression of exciton transition probability matrix A is as follows:

symmetry of the nanoarray **C1**$_N$, $x_1(t) = x_{2N}(t)$, such that we focused on $x_1(t)$ here. We assume that the initial state of the exciton distribution in **C1**$_N$ is $\boldsymbol{x}(t=0) = \frac{1}{2N-2}(0,1,1,\cdots,1,1,0)^T$, and that the exciton initially appears at any of the $2N-2$ dipyrrin sites of **BL3** with equal probability, being an ensemble average of all possible initial states. $x_i(t)$ at any time t can be obtained by solving Eq. 2. To save computational resources, Eq. 2 was decomposed as follows:

$$\frac{d}{dt}\begin{pmatrix} x_1(t) \\ \vec{X}(t) \\ x_{2N}(t) \end{pmatrix} = \begin{pmatrix} A_{1,1} & \vec{a}^T & 0 \\ 0 & A' & 0 \\ 0 & \vec{a}'^T & A_{2N,2N} \end{pmatrix}\begin{pmatrix} x_1(t) \\ \vec{X}(t) \\ x_{2N}(t) \end{pmatrix} \tag{11}$$

Here, A' is a submatrix of A consisting of $A_{i,j}$ ($2 \le i, j \le 2N-1$). A' is a symmetric matrix because it denotes only the reversible exciton transfers within the **BL3** chain, except for its diagonal elements. $\vec{X}(t) = (x_2(t), \ldots, x_{2N-1}(t))$. $\vec{a}^T = (A_{1,2}, \ldots, A_{1,2N-1})$. $\vec{a}'^T = (A_{2N,2}, \ldots, A_{2N,2N-1})$. Due to the symmetry of A', an orthogonal matrix P satisfies $PA'P^T = J$. Here, J is a diagonal matrix whose diagonal elements are the eigenvalues of A'. Given the centrosymmetry of A and $\boldsymbol{x}(0)$, $x_1(t) = x_{2N}(t)$ is calculated as follows.

$$x_1(t) = x_1(0)e^{A_{1,1}t} + \vec{a}^T P^T \frac{e^{Jt} - e^{A_{1,1}t}I}{J - A_{1,1}I}P\vec{X}(0) \tag{12}$$

Here I is the identity matrix. A normalized PL decay curve may be simulated by convoluting $x_1(t)$ with the instrument response function of the PL lifetime measurement apparatus (Supplementary Fig. 65). We simulated the PL decay curves for $N = 2–16$ and compared them with the normalized experimental data. Since $x_1(t)$ includes $k_{h\text{-end}}$ and $k_{h\text{-in}}$, these were set as fitting parameters, and $k_{h\text{-end}}$ and $k_{h\text{-in}}$ that best reproduced the fluorescence decay curves for all N were obtained by the least squares method (Supplementary Figs. 50–52). The errors for $k_{h\text{-end}}$ and $k_{h\text{-in}}$ were set to include the range in which the residual sums of squares were less than or equal to 1.05 times the minimum values (Supplementary Fig. 66). The series of simulation and fitting was performed independently for three solvents (toluene, a mixture of toluene/DCM (1:1 v/v), and DCM).

$$A = \begin{pmatrix} -k_{r-\textbf{L1}} - k_{nr-\textbf{L1}} & k_{h-end} & 0 & k_{F[4,1]} & k_{F[5,1]} & 0 \\ 0 & -k_{r-\textbf{BL3}} - k_{nr-\textbf{BL3}} - \sum_{i\neq2}A_{i2} & k_{F[3,2]} & 0 & 0 & 0 \\ 0 & k_{F[2,3]} & -k_{r-\textbf{BL3}} - k_{nr-\textbf{BL3}} - \sum_{i\neq3}A_{i3} & k_{h-in} & 0 & 0 \\ 0 & 0 & k_{h-in} & -k_{r-\textbf{BL3}} - k_{nr-\textbf{BL3}} - \sum_{i\neq4}A_{i4} & k_{F[5,4]} & 0 \\ 0 & 0 & 0 & k_{F[4,5]} & -k_{r-\textbf{BL3}} - k_{nr-\textbf{BL3}} - \sum_{i\neq5}A_{i5} & 0 \\ 0 & k_{F[2,6]} & k_{F[3,6]} & 0 & k_{h-end} & -k_{r-\textbf{L1}} - k_{nr-\textbf{L1}} \end{pmatrix} \tag{10}$$

Among the matrix element of A, $k_{h\text{-end}}$ and $k_{h\text{-in}}$ were unknown parameters, which were shared among different N but not shared between different solvents. $k_{h\text{-end}}$ and $k_{h\text{-in}}$ were determined by the procedure below.

The experimental PL decay curves of **C1**$_N$ (Fig. 4e-g and Supplementary Figs. 50–52) were recorded upon 470 nm excitation, i.e., the excitation of either dipyrrin site of **BL3**. As can be seen from the steady-state PL spectra (Fig. 3h and Supplementary Figs. 36b, 37b), the contribution of the emission from **L1** at 579 nm is dominant in this case. This is due to the efficient exciton transfer from the dipyrrin site of **BL3** to **L1**, and the PLQY of the dipyrrin site of **BL3** is much smaller than that of **L1** (Supplementary Tables 4,5,7–9). Therefore, the PL intensity at time t is proportional to the probability of the exciton presence at dipyrrin sites 1 and $2N$, $x_1(t)$ and $x_{2N}(t)$. Also, due to the

The ϕ_{PL_490} value, the PLQY of **C1**$_N$ excited at 490 nm, is simulated as follows:

$$\begin{aligned} \phi_{PL\_490} &= \int_0^\infty dt\, \boldsymbol{k}^T \boldsymbol{x}(t) \\ &= \int_0^\infty dt\, \boldsymbol{k}^T \exp[tA]\boldsymbol{x}(t=0) \\ &= -\boldsymbol{k}^T A^{-1} \boldsymbol{x}(t=0) \end{aligned} \tag{13}$$

where $\boldsymbol{k}^T = (k_{r-\textbf{L1}}, k_{r-\textbf{BL3}} \ldots k_{r-\textbf{BL3}}, k_{r-\textbf{L1}})$ is a $2N$-dimensional row vector of the radiative decay rate constants of dipyrrin sites 1, 2…2N. The initial state of the exciton distribution in **C1**$_N$ is $\boldsymbol{x}(t=0) = \frac{1}{2N-2}(0,1,1,\cdots,1,1,0)^T$, the same as the simulation of the PL

decay curve. Using Eq. 13, we calculated ϕ_{PL_490} for $N = 2$–16 via $k_{h\text{-end}}$ and $k_{h\text{-in}}$ that were obtained so that the PL decay curves are best reproduced. Note that experimental ϕ_{PL_554} obtained when **L1** was directly excited at 554 nm, showed a slight N dependence (Fig. 4a-c; Supplementary Tables 4 and 5), such that we considered this dependence also in the simulation of ϕ_{PL_490}. The simulation of ϕ_{PL_490} was performed independently for the three solvents (toluene, a mixture of toluene/DCM (1:1 v/v), and DCM). We confirmed that the optimal values of $k_{h\text{-end}}$ and $k_{h\text{-in}}$ obtained by the PL decay curve fitting also reproduced the experimental ϕ_{PL_490}–N plot in every three solvent (Fig. 4k-m).

Data availability

Crystallographic data for the structure reported in this article have been deposited at the Cambridge Crystallographic Data Centre under deposition number CCDC 2386878. These data can be obtained free of charge from The Cambridge Crystallographic Data Center via www.ccdc.cam.ac.uk/data_request/cif. The optimized computational structures reported in this article are provided in Source data section. All other data supporting the findings of this study are available within the article and its Supplementary Information, or from the corresponding author upon request. Source data are provided with this paper.

References

1. Pearson, K. The problem of the random walk. *Nature* **72**, 294 (1905).
2. Fama, E. F. Random walks in stock market prices. *Financ. Anal. J.* **21**, 55–59 (1965).
3. Pinsky, M. A. & Karlin, S. *An Introduction to Stochastic Modeling* 3rd edn (Elsevier Inc., 2011).
4. Masuda, N. Random walks and diffusion on networks. *Phys. Rep.* **716–717**, 1–58 (2017).
5. Simpson, O. Electronic properties of aromatic hydrocarbons III. Diffusion of excitons. *Proc. Roy. Soc. A* **238**, 402–411 (1957).
6. Montroll, E. W. Random walks on lattices. III. Calculation of first-passage times with application to exciton trapping on photosynthetic units. *J. Math. Phys.* **10**, 753–765 (1968).
7. Rosenstock, H. B. Luminescent emission from an organic solid with traps. *Phys. Rev.* **187**, 1166 (1969).
8. Soos, Z. G. & Powell, R. C. Generalized random-walk model for singlet-exciton energy transfer. *Phys. Rev. B* **6**, 4035–4046 (1972).
9. Fitzgibbon, P. D. & Frank, C. W. Energy migration in the aromatic vinyl polymers. 1. A one-dimensional random walk model. *Macromolecules* **15**, 733–741 (1982).
10. Keller, J. M. et al. Negative polaron and triplet exciton diffusion in organometallic "molecular wires. *J. Am. Chem. Soc.* **133**, 11289–11298 (2011).
11. Li, M. et al. Triplet–triplet energy transfer inside the single organic nanocrystal revealed by microscopic time resolved spectroscopy. *J. Phys. Chem. C* **126**, 11033–11041 (2022).
12. Zhang, Q. et al. Förster energy transport in metal–organic frameworks is beyond step-by-step hopping. *J. Am. Chem. Soc.* **138**, 5308–5315 (2016).
13. Toyoda, R. et al. A single-stranded coordination copolymer affords heterostructure observation and photoluminescence intensification. *Sci. Adv.* **5**, eaau0637 (2019).
14. Loudet, A. & Burgess, K. BODIPY dyes and their derivatives: syntheses and spectroscopic properties. *Chem. Rev.* **107**, 4891–4932 (2007).
15. Ulrich, G., Ziessel, R. & Harriman, A. The chemistry of fluorescent bodipy dyes: versatility unsurpassed. *Angew. Chem. Int. Ed.* **47**, 1184–1201 (2008).
16. Boens, N., Leen, V. & Dehaen, W. Fluorescent indicators based on BODIPY. *Chem. Soc. Rev.* **41**, 1130–1172 (2012).
17. Li, F. et al. Design, synthesis, and photodynamics of light-harvesting arrays comprised of a porphyrin and one, two, or eight boron-dipyrrin accessory pigments. *J. Am. Chem. Soc.* **120**, 10001–10017 (1998).
18. Toyoda, R. et al. Synergistic interplay between photoisomerization and photoluminescence in a light-driven rotary molecular motor. *Nat. Commun.* **13**, 5765 (2022).
19. Hou, J., Toyoda, R., Meskers, S. C. J. & Feringa, B. L. Programming and dynamic control of the circular polarization of luminescence from an achiral fluorescent dye in a liquid crystal host by molecular motors. *Angew. Chem. Int. Ed.* **61**, e202206310 (2022).
20. Matsuoka, R. et al. Bis(dipyrrinato)metal(II) coordination polymers: crystallization, exfoliation into single wires, and electric conversion ability. *Chem. Sci.* **6**, 2853–2858 (2015).
21. Aoki, R. et al. Bis(dipyrrinato)zinc(II) complex chiroptical wires: exfoliation into single strands and intensification of circularly polarized luminescence. *J. Am. Chem. Soc.* **139**, 16024–16027 (2017).
22. Sakamoto, R. et al. Dissymmetric Bis(dipyrrinato)zinc(II) complexes: rich variety and bright red to near-infrared luminescence with a large pseudo-stokes shift. *J. Am. Chem. Soc.* **138**, 5666–5677 (2016).
23. Kusaka, S., Sakamoto, R., Kitagawa, Y., Okumura, M. & Nishihara, H. An extremely bright heteroleptic Bis(dipyrrinato)zinc(II) complex. *Chem. Asian J.* **7**, 907–910 (2012).
24. Toyoda, R. et al. Heteroleptic Bis(dipyrrinato)copper(II) and nickel(II) complexes. *Dalton Trans.* **44**, 15103–15106 (2015).
25. Kögel, J. F. et al. Heteroleptic [Bis(oxazoline)](dipyrrinato)zinc(II) complexes: bright and circularly polarized luminescence from an originally achiral dipyrrinato ligand. *Angew. Chem. Int. Ed.* **55**, 1377–1381 (2015).
26. Klärner, G., Davey, M. H., Chen, W.-D., Scott, J. C. & Miller, R. D. Colorfast blue-light-emitting random copolymers derived from Di-n-hexylfluorene and anthracene. *Adv. Mater.* **10**, 993–997 (1998).
27. Furuta, P. T., Deng, L., Garon, S., Thompson, M. E. & Fréchet, J. M. J. Platinum-functionalized random copolymers for use in solution-processable, efficient, near-white organic light-emitting diodes. *J. Am. Chem. Soc.* **126**, 15388–15389 (2004).
28. Jiang, J.-M. et al. Conjugated random copolymers of benzodithiophene–benzooxadiazole–diketopyrrolopyrrole with full visible light absorption for bulk heterojunction solar cells. *Polym. Chem.* **4**, 5321–5328 (2013).
29. Kim, S., Wang, H. S., Choe, Y., Choi, S.-H. & Bang, J. Controlling the microdomain orientation in block copolymer thin films via cross-linkable random copolymer neutral layer. *Polym. J.* **48**, 333–340 (2016).
30. Hosoyamada, M., Yanai, N., Okumura, K., Uchihashi, T. & Kimizuka, N. Translating MOF chemistry into supramolecular chemistry: soluble coordination nanofibers showing efficient photon upconversion. *Chem. Commun.* **54**, 6828–6831 (2018).
31. Chen, P.-J. et al. A ligand design with a modified naphthyridylamide for achieving the longest EMACs: the 1st single-molecule conductance of an undeca-nickel metal string. *Chem. Commun.* **53**, 4673–4676 (2017).
32. Ismayilov, R. H. et al. Two linear undecanickel mixed-valence complexes: increasing the size and the scope of the electronic properties of nickel metal strings. *Angew. Chem. Int. Ed.* **50**, 2045–2048 (2011).
33. Tanaka, K. et al. Programmable self-assembly of metal ions inside artificial DNA duplexes. *Nat. Nanotechnol.* **1**, 190–194 (2006).
34. Horiuchi, S. et al. Multinuclear metal-binding ability of a carotene. *Nat. Commun.* **6**, 6742 (2015).
35. Yamamoto, Y. et al. Systematic synthesis, isolation, and photophysical properties of linear-shaped Re(I) oligomers and polymers with 2-20 units. *J. Am. Chem. Soc.* **130**, 14659–14674 (2008).
36. Patalag, L. J., Hoche, J., Mitric, R., Werz, D. B. & Feringa, B. L. Transforming dyes into fluorophores: exciton-induced emission with chain-like oligo-BODIPY superstructures. *Angew. Chem. Int. Ed.* **61**, e202116834 (2022).

37. Maeda, H. et al. Nanoscale spherical architectures fabricated by metal coordination of multiple dipyrrin moieties. *J. Am. Chem. Soc.* **128**, 10024–10025 (2006).

38. Wood, T. E. & Thompson, A. Advances in the chemistry of dipyrrins and their complexes. *Chem. Rev.* **107**, 1831–1861 (2007).

39. Baudron, S. A. Luminescent dipyrrin based metal complexes. *Dalton Trans.* **42**, 7498–7509 (2013).

40. Trinh, C. et al. Symmetry-breaking charge transfer of visible light absorbing systems: zinc dipyrrins. *J. Phys. Chem. C* **118**, 21834–21845 (2014).

41. Momeni, M. R. & Brown, A. Why do TD-DFT excitation energies of BODIPY/Aza-BODIPY families largely deviate from experiment? answers from electron correlated and multireference Methods. *J. Chem. Theory Comput.* **11**, 2619–2632 (2015).

42. Norris, J. R. *Markov Chains* (Cambridge University Press, 1998).

43. Mikhnenko, O. V. et al. Exciton diffusion in organic semiconductors. *Energy Environ. Sci.* **8**, 1867 (2015).

44. Petrov, D., Shkuratov, Y. & Videen, G. Optimized matrix inversion technique for the *T*-matrix method. *Opt. Lett.* **32**, 1168–1170 (2007).

45. Hellenkamp, B. et al. Precision and accuracy of single-molecule FRET measurements—a multi-laboratory benchmark study. *Nat. Methods* **15**, 669–676 (2018).

Author contributions

R.S. and R.T. initiated the present work, and R.S. and H.N. directed it. R.T., J.K., Ha.T. and Y.C. conducted the synthesis of the ligands and the multinuclear complexes and performed photophysical measurements. N.F. conducted numerical calculations. H.U. performed theoretical investigations. Hi.T. and R.T. performed mass spectrometry for the multinuclear complexes. All the authors contributed to the manuscript preparation.

Competing interests

The authors declare no competing interests.

Additional information

Supplementary information The online version contains supplementary material available at https://doi.org/10.1038/s41467-025-56381-0.

Correspondence and requests for materials should be addressed to Ryojun Toyoda, Naoya Fukui or Ryota Sakamoto.

Peer review information *Nature Communications* thanks the anonymous reviewers for their contribution to the peer review of this work. A peer review file is available.

Reprints and permissions information is available at http://www.nature.com/reprints

Publisher's note Springer Nature remains neutral with regard to jurisdictional claims in published maps and institutional affiliations.